

Alkali-activation of CaO-FeOx-SiO₂ slag: Formation mechanism from in-situ X-ray total scattering

Peys, Arne; White, C. E.; Rahier, H.; Blanpain, B.; Pontikes, Yiannis

Published in:
Cement and Concrete Research

DOI:
[10.1016/j.cemconres.2019.04.019](https://doi.org/10.1016/j.cemconres.2019.04.019)

Publication date:
2019

License:
CC BY-NC-ND

Document Version:
Accepted author manuscript

[Link to publication](#)

Citation for published version (APA):
Peys, A., White, C. E., Rahier, H., Blanpain, B., & Pontikes, Y. (2019). Alkali-activation of CaO-FeOx-SiO₂ slag: Formation mechanism from in-situ X-ray total scattering. *Cement and Concrete Research*, 122, 179-188.
<https://doi.org/10.1016/j.cemconres.2019.04.019>

Copyright

No part of this publication may be reproduced or transmitted in any form, without the prior written permission of the author(s) or other rights holders to whom publication rights have been transferred, unless permitted by a license attached to the publication (a Creative Commons license or other), or unless exceptions to copyright law apply.

Take down policy

If you believe that this document infringes your copyright or other rights, please contact openaccess@vub.be, with details of the nature of the infringement. We will investigate the claim and if justified, we will take the appropriate steps.

Alkali-activation of CaO-FeO_x-SiO₂ slag: Formation mechanism from in-situ X-ray total scattering

A. Peys^{1,2}, C. E. White², H. Rahier³, B. Blanpain¹, Y. Pontikes¹

¹KU Leuven Department of Materials Engineering, Kasteelpark Arenberg 44, 3001 Leuven, Belgium.

²Department of Civil and Environmental Engineering, and the Andlinger Center for Energy and the Environment, Princeton University, Princeton, NJ 08544, USA.

³Department of Materials and Chemistry, Vrije Universiteit Brussel, Pleinlaan 2, 1050 Brussels, Belgium.

Abstract

The pursuit of low-CO₂ technologies has led to a surge in research on alternative cementitious materials, of which alkali-activated materials are a large family. In recent years alkali-activated materials have expanded to encompass Fe-rich precursors in addition to the more commonly employed aluminosilicate precursors. The formation mechanism of alkali-activated materials from two Fe-rich synthetic slags has been assessed by employing *in-situ* X-ray total scattering and subsequent pair distribution function analysis. The evolution of the local atom-atom correlations reveals three reaction stages. After the dissolution of Fe-silicate clusters from the slag, a binder phase is formed with Fe in both Fe²⁺ and Fe³⁺ oxidation states. The Fe²⁺ state is present in the form of trioctahedral layers, similar to those in Fe(OH)₂, while the Fe³⁺ is likely located in the polymerized silicate network. Exposure to air causes the Fe²⁺ species to transition to the Fe³⁺ state.

Keywords

Alkali-activation; inorganic polymers; in-situ X-ray pair distribution function; amorphous; Fe-silicate

Introduction

Determination of the formation mechanism of the binders in cement-based materials is key for understanding their early-age chemical and physical properties and associated long-term performance.

Over the last couple of decades, there has been increasing interest in the use of novel alternative cements to decrease the environmental footprint associated with Portland cement production [1-3]. With the Portland cement industrial sector accounting for 5-9% of global anthropogenic CO₂ emissions due to ~4 Gt of yearly production, there is an overwhelming need to enhance the use of sustainable alternatives [3,4]. Alkali-activated materials (AAMs) and inorganic polymers (IPs) are popular alternative cements [1,2,5] which have recently received a boost of interest in research and at a larger commercial scale [6,7]. These materials are synthesized by mixing a solid silicate with a source of alkali, such as sodium/potassium hydroxides or silicates. The formation mechanism of IPs synthesized using an aluminosilicate precursor, in which two types of chemical reactions take place - dissolution (alkaline hydrolysis) and polymerization (polycondensation) - is quite well-known [8-10]. The polymerization reactions can be further divided into 'gelation', 'reorganization' and 'polymerization and hardening' according to the state of the aluminosilicate network [11,12].

Prior to discussing Fe-rich residues and their behavior in alkali-activated systems, the reaction mechanism of the more commonly studied aluminosilicate residues is elaborated. During dissolution of the aluminosilicate precursor, aluminosilicate and silicate oligomeric species are liberated from the solid [13], where the rate of aluminate release from the precursor has been shown to affect the homogeneity of the microstructure of the resulting binder [14]. The overall rate of dissolution is largely controlled by the precursor molecular/ionic structure [15,16], the alkalinity of the activating solution [15,17,18] and the particle size of the precursor [19]. Once species are released into solution, they undergo polycondensation reactions to form larger aluminosilicate oligomers/nanoprecipitates dependent on the solution concentration and pH [12,13,20,21]. An aluminosilicate three-dimensional network is created once the solution is supersaturated with respect to the aluminosilicate species, where aluminates are in tetrahedral configuration (charge balanced by the alkali, typically Na/K) [6,7,22]. Furthermore, for metakaolin-based IPs the topology of the aluminosilicate network has been seen to consist of four-membered rings [20]. Growth of the aluminosilicate network has been studied using coarse-grained Monte Carlo simulations, where for both metakaolin- and fly ash-based IPs the growth process depends on the activator chemistry. For hydroxide-activated IPs the network emerges via growth of many

aluminosilicate particles that ultimately coalesce to form the three-dimensional network. For silicate-activated systems, growth is seen to follow an **Ostwald** ripening-type process, in which, after aluminosilicate particles have been established in the system, the larger particles grow at the expense of the smaller ones through dissolution/re-precipitation [12,23]. During this later stage of reaction, hardening occurs together with an increase in the connectivity of the aluminosilicate network [13,24]. Subtle longer-term changes to the network have been observed, specifically a slight increase in atomic ordering [25].

There are numerous industrial residues that contain large quantities of Fe. **These residues mainly consider slags from non-ferrous metallurgy, but there are also other sources such as steelmaking slags [26] or bauxite residues [27], where a significant fraction of Fe is observed.** It is only within the last decade that **the use of Fe-rich precursors** in AAMs has been **more extensively** investigated; the literature reports varying mechanical performance and the development of a water insoluble silicate-based binder [28-32]. These results are promising, particularly given the lower environmental footprint of these binders. Compared to Portland cement-based systems, the environmental impact single score, i.e. aggregation of all midpoint categories, of AAMs synthesized using Fe-rich residues, is lower by as much as 77%, while CO₂ emissions are reduced by up to 83% [33]. **These values are mixture specific and not an AAM system property. The work of Habert et al. [34] for instance reports less positive data when using metakaolin as precursor and more concentrated alkaline solutions.** From a formation mechanism viewpoint, these Fe-rich AAMs follow a similar reaction sequence to aluminosilicate IPs, in which dissolution is followed by an exothermic peak around the time of setting, associated with polycondensation [18,30]. During this process, however, Fe changes oxidation state from II to III [35-38], which, according to *ex-situ* ⁵⁷Fe Mössbauer spectroscopy, is seen to occur in parallel with the polymerization reaction [39]. The Fe³⁺-based reaction product has an average coordination number of 4-5 [37,38] and possesses atomic correlations that are similar to the precursor slag [40].

This investigation elaborates on the knowledge obtained in these previous works, by providing details of the molecular structure and its evolution over time, beyond the oxidation state and coordination number of Fe. The study uses *in-situ* high-energy X-ray total scattering to elucidate the atomic evolution

of Fe-rich AAMs during the early stages of reaction and to unravel the formation mechanism of the binder. This has been achieved by tracking the evolution of the total scattering data and pair distribution function (PDF) during the initial 80 hours reaction, where the speciation of the intermediate reaction products in solution has been identified together with the atomic arrangements of any metastable phases. The kinetics of individual reaction types have been studied via tracking of specific atom-atom correlations in the PDF data and the small-angle region in the reciprocal-space data. Finally, the impact on the formation mechanism and resulting atomic structure of the alkali-activated binder of both precursor composition (Fe/Ca molar ratio) and alkali metal in the activating solution (Na/K) have been determined.

Material and methods

Two Fe-rich slags have been investigated, a “low-Ca” and a “high-Ca” slag, as outlined in previous work [40], which have approximate molar compositions of $0.83\text{FeO-SiO}_2\text{-}0.17\text{CaO}$ and $0.67\text{FeO-SiO}_2\text{-}0.33\text{CaO}$, respectively. The production of the slags was performed by melting oxide powders and water quenching the molten slag, using the methodology of previous work [38]. In this procedure, Fe, Fe_2O_3 , SiO_2 and CaO powders are mixed and a melt is produced in an Indutherm TF4000 using a steel crucible at a temperature 100 °C above the liquidus temperature. This temperature is calculated using FactSage software (version 7.0). The change in chemical composition of the slag that occurs during production due to dissolution of the steel crucible was taken into account in these calculations. After obtaining a completely molten phase, a mixture of CO/CO₂ (flow of 40/20 L/h) is bubbled through the melt for a duration of 15 minutes. Quenching is carried out by transferring the liquid slag to a water bucket using a stainless steel ladle. The activators were a sodium silicate solution (molar ratios $\text{SiO}_2/\text{Na}_2\text{O} = 1.6$ and $\text{H}_2\text{O}/\text{Na}_2\text{O} = 20$) and a potassium silicate solution (molar ratios $\text{SiO}_2/\text{K}_2\text{O} = 1.6$ and $\text{H}_2\text{O}/\text{K}_2\text{O} = 20$). These solutions were made by first dissolving the hydroxide (Sigma-Aldrich, 97.0 (NaOH) and 85 wt.% (KOH) purity) in distilled water, and then mixing with fumed silica (Sigma-Aldrich, 99.8 wt% purity). The silica-rich solutions were allowed to equilibrate for 48 hours. Pastes consisting of the activating solution and Fe-rich slag were mixed for 10 seconds by hand followed by 1 minute using a Fisher Scientific Vortex mixer, maintaining a water/slag mass ratio of 0.28 (solution/slag mass ratio was 0.40

for Na, 0.43 for K-silicate solution). For each X-ray scattering sample, the paste was loaded via suction into a 1 mm diameter polyimide capillary and both ends were sealed using modeling clay.

X-ray scattering experiments were performed at the Advanced Photon Source, Argonne National Laboratory, on beamline 11-ID-B using a monochromatic X-ray energy of 58.66 keV. *In-situ* scans were acquired for each sample every 10 minutes, starting at 15 minutes after mixing and ending after 15 hours. After these *in-situ* scans, the same samples were re-measured at 27, 40, 62 and 81 hours. A scan time of 2 minutes per sample was used along with a sample-detector distance of 180 mm. The 2D diffraction data were integrated using GSASII (intensity calibrated with respect to CeO₂). Calculation of the scattering function ($S(Q)$) and the Fourier transform, used to obtain the PDF ($G(r)$) in real space, were performed using PDFgetX2 [41], with a Q_{\min} of 0.9 Å⁻¹ and Q_{\max} of 20 Å⁻¹. Simulated PDFs of the crystalline phases have been generated using PDFgui [42].

Results and discussion

Evolution in reciprocal space

An example scattering function is provided in Figure 1, showing the data for the Na-activated high-Ca slag at different stages of the reaction. The most pronounced change as a function of reaction time is the intensity increase at 0.3-0.4 Å⁻¹. This is the high-Q region of the small-angle scattering (SAS) intensity, which is cut off by the beam stop for the current X-ray total scattering setup to avoid oversaturation of the detector. The maximum intensity cannot be directly related to the nanoscale morphology of the material, therefore, but instead will be a combination of scattering from the material and contributions from the experimental setup. By examining SAS data from the literature for AAMs [43-45], however, the intensity at 0.3-0.4 Å⁻¹ can be used to qualitatively analyze the formation of pores or a layered structure in the paste as it evolves. Although previous studies on metakaolin-based IPs have shown that this SAS region is attributed to pores in the paste [43], a layered structure cannot be discounted at this stage of the investigation as calcium-silicate-hydrate-type gels typical of Portland cements and Ca-rich AAMs/IPs can give rise to a basal peak in reciprocal space positioned between $\sim 0.35 \leq Q \leq 0.8$ [46]. The minor differences at higher Q values (1-10 Å⁻¹) are shown more clearly by the difference plot given

in Figure 1. The broad diffuse peaks in this figure show that the changes occurring during reaction are attributed to slag dissolution together with the formation of amorphous reaction products. In general, the *in-situ* total scattering functions of all samples have a similar appearance (see supplementary data) as the reactions progress and are close to those of the ex-situ samples from previous work [40].

A comparison of the *in-situ* total scattering data after 62 hours for Na-activated low-Ca slag, with a sample of the same chemical composition that was extensively cured (61 days in a closed bottle), milled and loaded in the capillary as a powder (> 6 months in age, the sample is from previous work and was remeasured on 11-ID-B in conjunction with the *in-situ* measurements [40]), shows that after 6 months the SAS region decreases in intensity, Figure 2. This suggests that the porosity or the layered features that emerge during the early stages of the reaction are disrupted after the extended curing period (including milling and exposure of the powder to air), indicating that (i) the layered features are associated with an intermediate reaction product, or (ii) the pore structure is significantly augmented during the later stages of reaction.

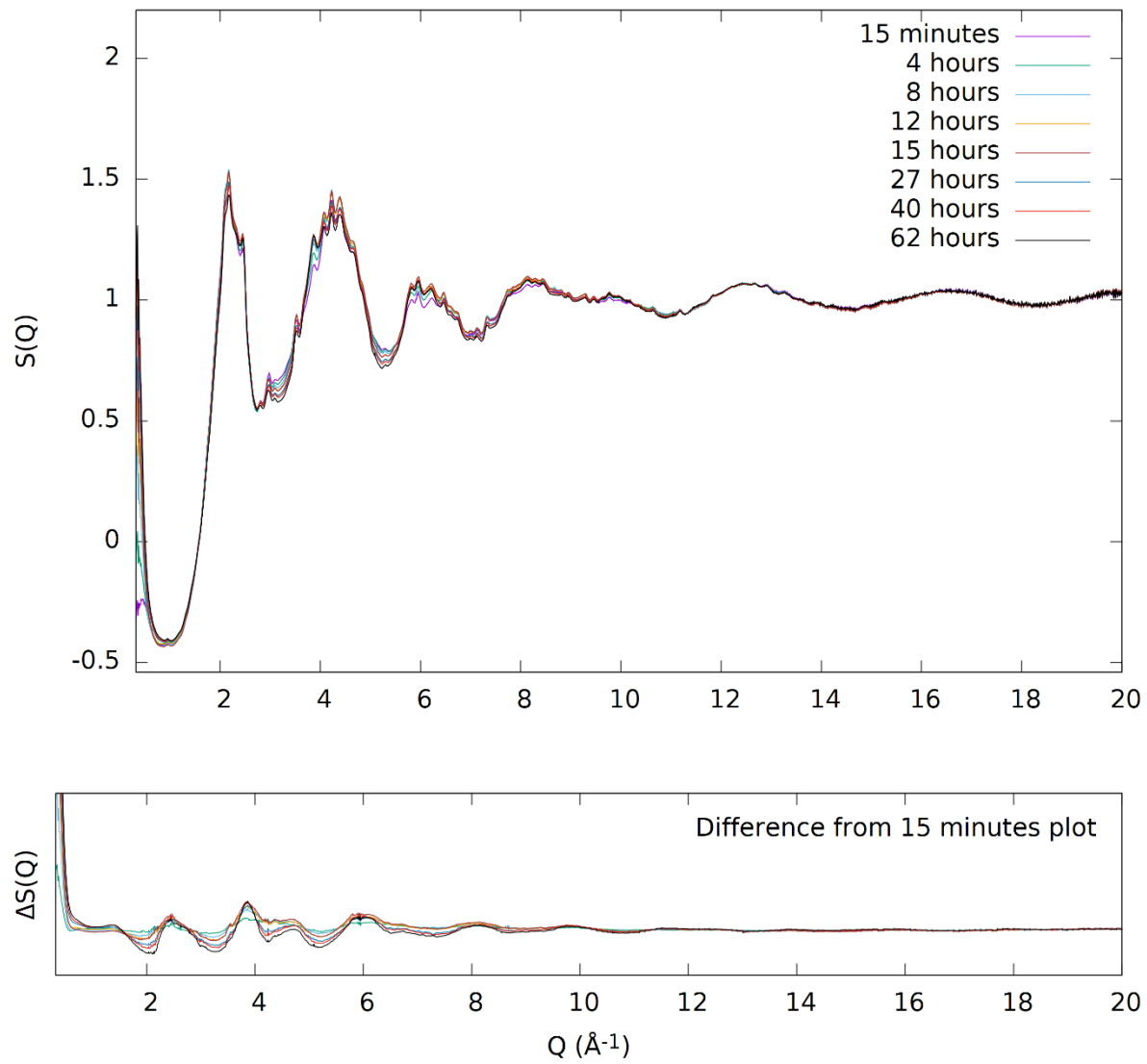


Figure 1: X-ray total scattering functions of Na-silicate activated high-Ca slag during the initial 62 hours of reaction. Upper plot: Full total scattering functions. Lower plot: Difference curves obtained by subtracting the initial data set (15 minutes) from those at later times.

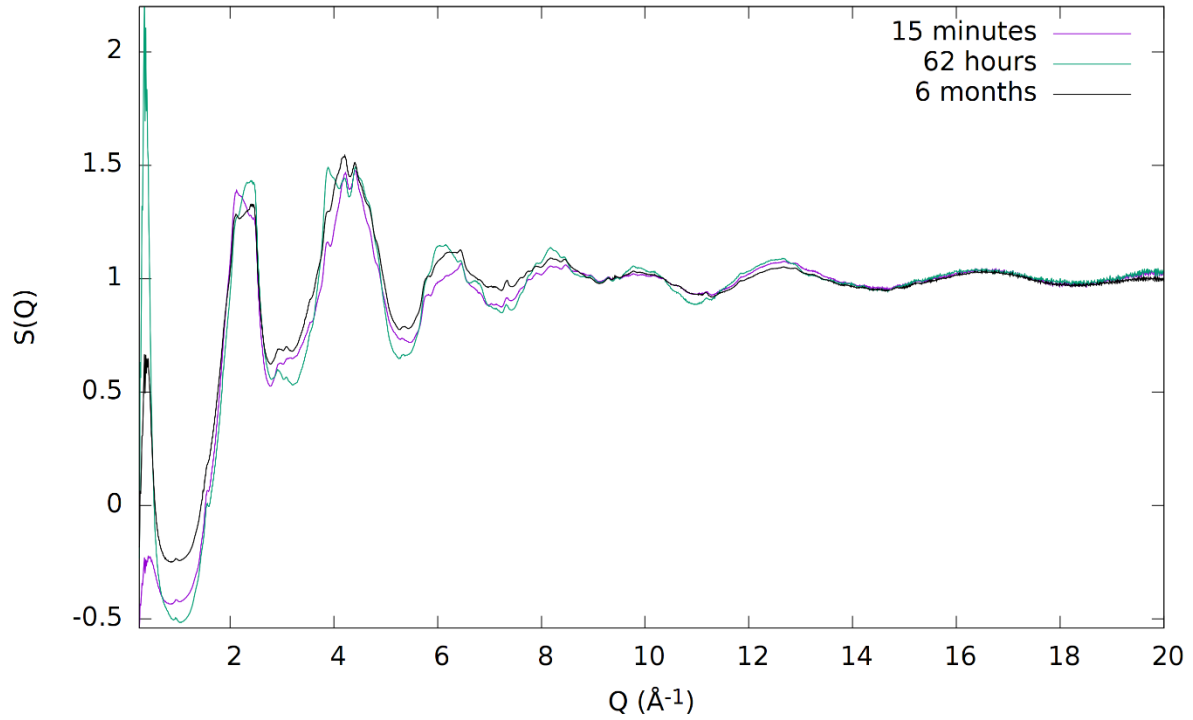


Figure 2: X-ray total scattering functions of Na-silicate activated low-Ca slag at 15 minutes, 62 hours and approx. 6 months after mixing. Note that the 6 months sample was cured in a sealed container, then crushed into a powder and loaded into a polyimide capillary prior to measurement.

The intensity of the SAS peak as a function of time during the *in-situ* measurements is plotted for all samples in Figure 3. After an induction period of approximately 2 hours, during which the intensity does not change, the binder structure starts to form. As mentioned previously, without complementary experimental data on the evolution of the pore structure of Fe-rich AAMs, it is difficult to assign these changes in the SAS intensity to a specific structural feature within the AAM. Figure 3 indicates that the reactions are occurring faster for the low-Ca slag (steeper slope), however, which may be a direct reflection of either faster reaction kinetics or that the AAM is forming (i) a more porous structure or (ii) a more ordered layered phase. Interestingly, setting of the Fe-rich slags occurs soon after the end of the induction period noted in Figure 3, typically ~3 hours after initial mixing.

In terms of the impact of the alkali (Na/K), there is a much stronger difference in the SAS region between sodium and potassium for the low-Ca systems compared with the high-Ca systems. While the Na-activated low-Ca sample is seen to initially react faster, which was also observed for metakaolin-based

geopolymers [43], the reaction rate for the K-activated low-Ca sample seems to catch up with the Na-activated sample during the later stages of reaction, specifically between ~27 and 40 hours after mixing. According to Steins et al. [47], this behavior is associated with the higher amount of mesopores in the final structure of K-activated aluminosilicate IPs. In the present work, this is difficult to confirm due to the decline in SAS intensity between 62 hours and ~6 months, as seen in Figure 2.

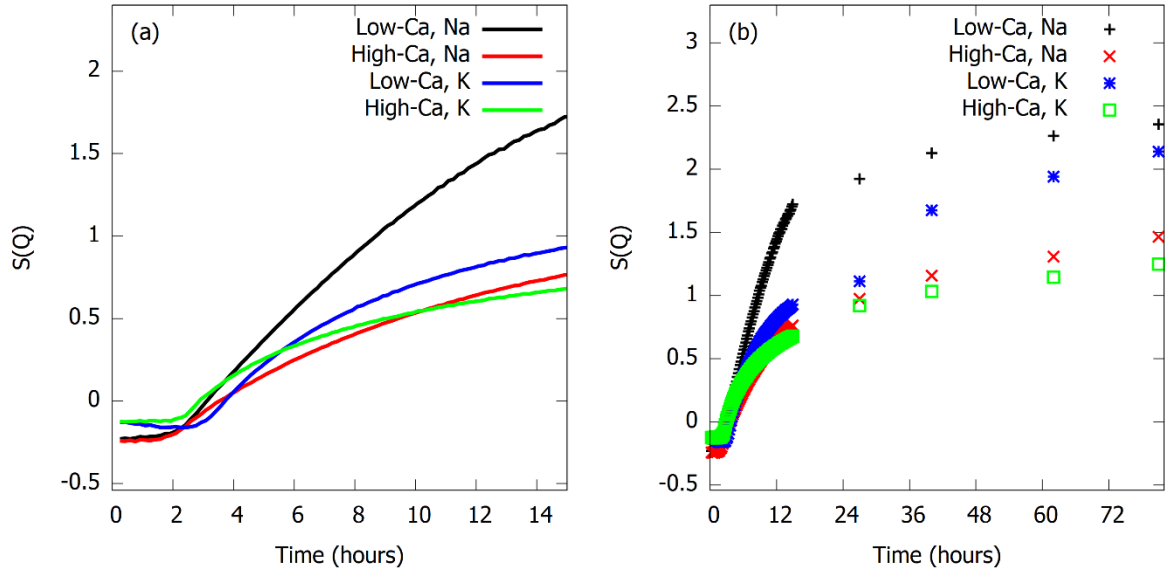


Figure 3: Evolution of the intensity of the small-angle region (maximum $S(Q)$ within a Q range of 0.3-0.4 \AA^{-1}) in the X-ray total scattering functions. (a) During the initial 15 hours of reaction and (b) up to 80 hours after initial mixing.

Evolution in real space

The PDF data are presented in Figures 4 to 7 for the Na-activated low-Ca slag, Na-activated high-Ca slag, K-activated low-Ca slag and K-activated high-Ca slag, respectively. The atom-atom correlations corresponding to specific peaks in the PDF data are indicated based on previous work on the slags and extensively cured samples [40]. The low- r correlations (Si-O, Fe-O, Ca-O and O-O) are denoted by vertical dashed lines, whereas higher- r correlations have been highlighted using a finite width to indicate the variation of the center of the Fe-metal correlation according to the oxidation state and coordination number of Fe. The center of the Fe-metal correlation can be located anywhere within this box, including the shoulders. To enable a better visual distinction between the Fe-Fe and Fe-Si boxes, different dash

types are used. For Na-silicate activated samples, the nearest-neighbor Na-O correlation is positioned at $\sim 2.3\text{-}2.5$ Å [20,40,48], which raises the intensity of the minimum between the Ca-O and O-O correlations, while the K-O correlation ($\sim 2.8\text{-}2.9$ Å [49]) exerts a similar influence on the intensity between the O-O and Fe-Fe correlations.

Taking into account previous X-ray absorption near-edge spectroscopy and Mössbauer spectroscopy data on Fe-rich slags with similar chemical compositions [38,39], the position of the nearest-neighbor Fe-O correlation (Figures 4 to 7; see also [40]) 15 minutes after initial mixing is indicative of the precursor slag, and contains a combination of IV- and V-fold coordinated Fe species. Furthermore, with respect to the local bonding environment and speciation of Fe in the AAMs, previous work [39] has shown that $^{\text{VI}}\text{Fe}^{2+}$ and $^{\text{IV}}\text{Fe}^{3+}$ species emerge simultaneously as the reaction continues. According to the Fe-O distances reported in the literature, this behavior should lead to an increase in intensity on either side of the Fe-O correlation associated with the slag (~ 2.02 Å), specifically the high r (~ 2.14 Å) and low r (~ 1.86 Å) shoulder for $^{\text{VI}}\text{Fe}^{2+}$ and $^{\text{IV}}\text{Fe}^{3+}$, respectively [40,48,50]. The inserts of Figures 4 and 6 show a shift of the Fe-O maximum intensity toward higher r values, confirming the emergence of $^{\text{VI}}\text{Fe}^{2+}$ species. The formation of $^{\text{IV}}\text{Fe}^{3+}$ is less evident, however. The isomer shifts associated with this species shown by Mössbauer spectroscopy were seen to be large [39], suggesting that the Fe-O bond lengths associated with this species will also be larger than commonly observed for a $^{\text{IV}}\text{Fe}^{3+}$ site [51]. Hence, instead of seeing an intensity rise at 1.86 Å, the $^{\text{IV}}\text{Fe}^{3+}\text{-O}$ is more likely to be positioned between 1.90 and 1.95 Å.

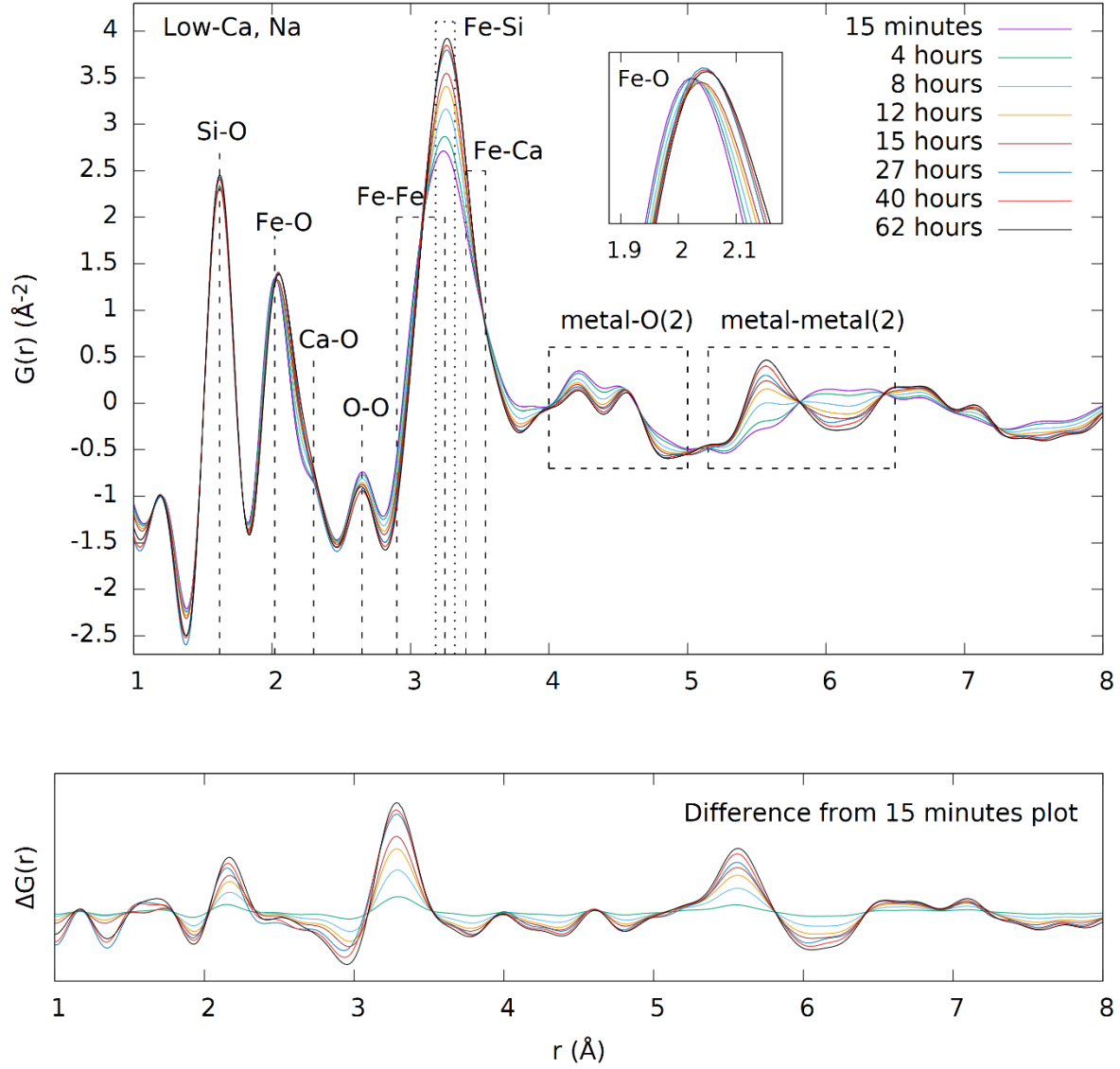


Figure 4: X-ray PDFs of the Na-silicate activated low-Ca slag during the initial 62 hours of reaction.

Upper plot: Full PDFs and insert showing a zoom of the Fe-O correlation. Lower plot: Difference curves obtained by subtracting the initial data set (15 minutes) from those at later times.

The evolution of the metal-metal correlations in the PDFs in Figures 4 to 7 is dominated by the rise in intensity of the main peak, denoted as the Fe-Si correlation at ~ 3.24 Å. The increase in distance between Fe and O upon formation of the $^{\text{VI}}\text{Fe}^{2+}$ should be considered, however, as it results in a potential Fe-Fe correlation at 3.25 Å [50]. The reason for this overall increase in the Fe-Si peak intensity and area as the reaction proceeds (Figures 4 to 7) has two possibilities. First, an increase in sample density would lead

to an increase in the atom-atom correlations, but as this would also affect the intensities of the nearest-neighbor bond lengths (such as Si-O) [52], and the PDF curves do not reflect such a change, density is not likely to be the cause of the increase in Fe-Si peak area. The second, and more probable, explanation is that the former Fe-Si correlation in the slag partially transitions toward a correlation that contains an element with a larger scattering cross-section, such as Fe-Fe or Fe-Ca [40]. Given that the Fe-Ca correlation is not usually observed around 3.25 Å [48,50], the rise in intensity is attributed to a Fe-Fe correlation. The position of 3.25 Å for the Fe-Fe correlation directly results from the Fe-O distance of 2.14 Å, and this rise in intensity of the metal-metal correlations should therefore be associated with the formation of a configuration with $^{VI}\text{Fe}^{2+}$. The elevated intensity of the Fe-Fe correlation suggests that this state contains an elevated amount of Fe-O-Fe linkages; thus, $^{VI}\text{Fe}^{2+}$ is not homogeneously distributed throughout the silicate network, but instead shows a preferential aggregation. This phenomenon is clearly observed in the low-Ca systems (Figures 4 and 6) but is less pronounced when more Ca (and less Fe) is present (Figures 5 and 7). The intensity of the curves where the Fe-Ca, Ca-Si and Ca-Ca correlations would be present (3.4-4.0 Å [47-56]) shows a drop as the reaction proceeds. This suggests that Ca does not take part in the formation of the binder during the early stages. Instead it may reside in the pore solution or be involved in a secondary phase (if present).

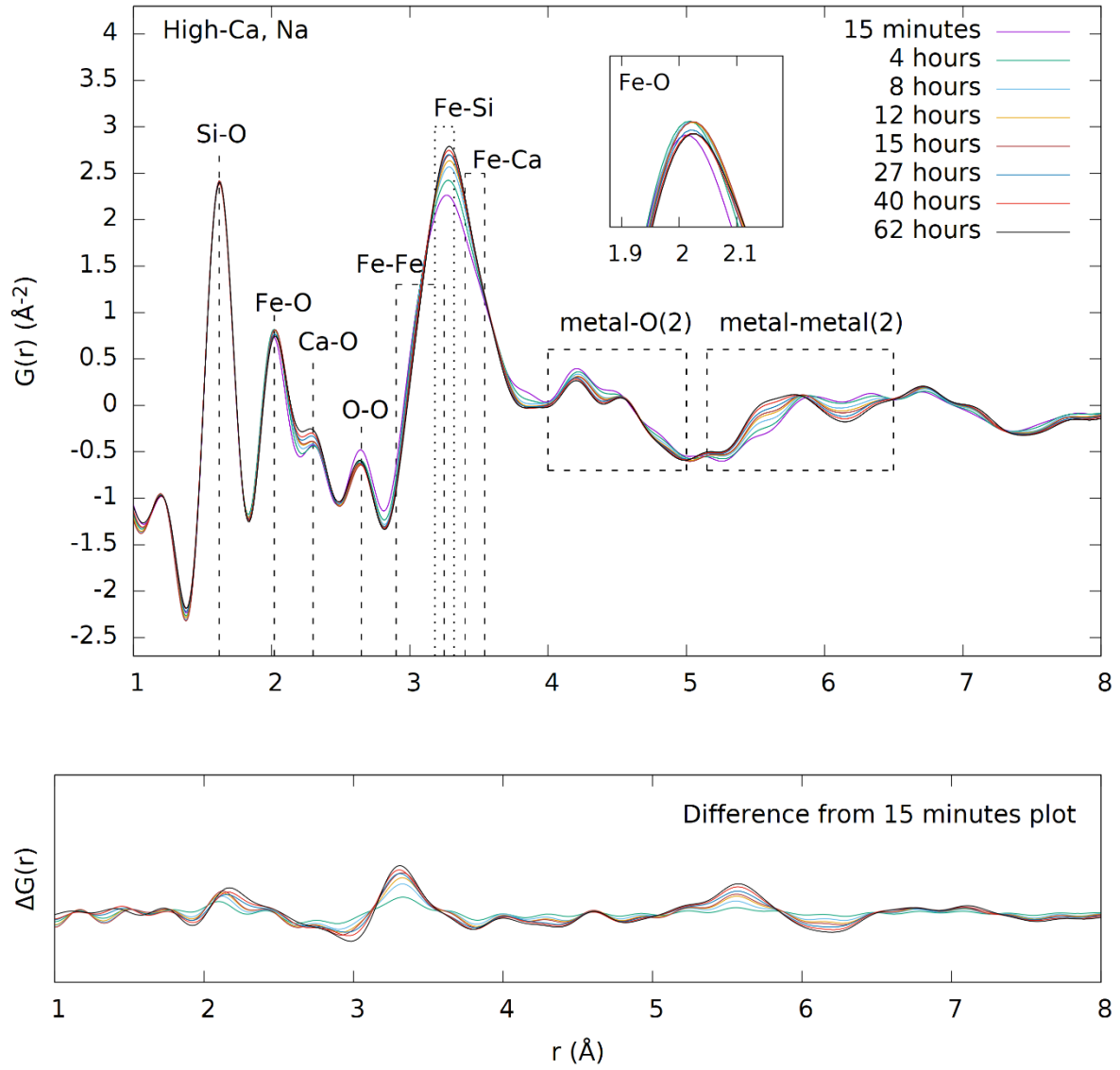


Figure 5: X-ray PDFs of the Na-silicate activated high-Ca slag during the initial 62 hours of reaction.

Upper plot: Full PDFs and insert showing a zoom of the Fe-O correlation. Lower plot: Difference curves obtained by subtracting the initial data set (15 minutes) from those at later times.

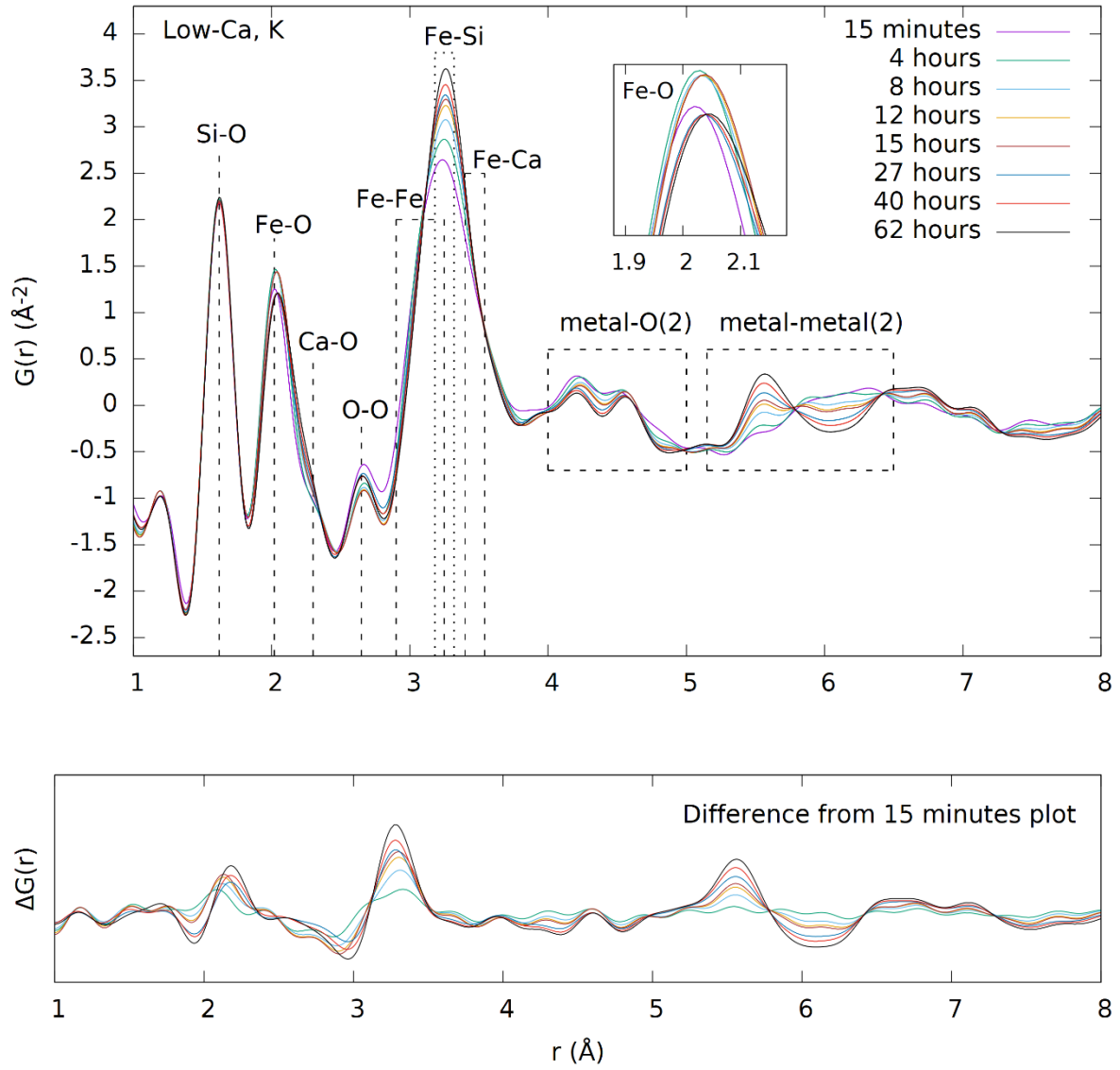


Figure 6: X-ray PDFs of the K-silicate activated low-Ca slag during the initial 62 hours of reaction.

Upper plot: Full PDFs and insert showing a zoom of the Fe-O correlation. Lower plot: Difference curves obtained by subtracting the initial data set (15 minutes) from those at later times.

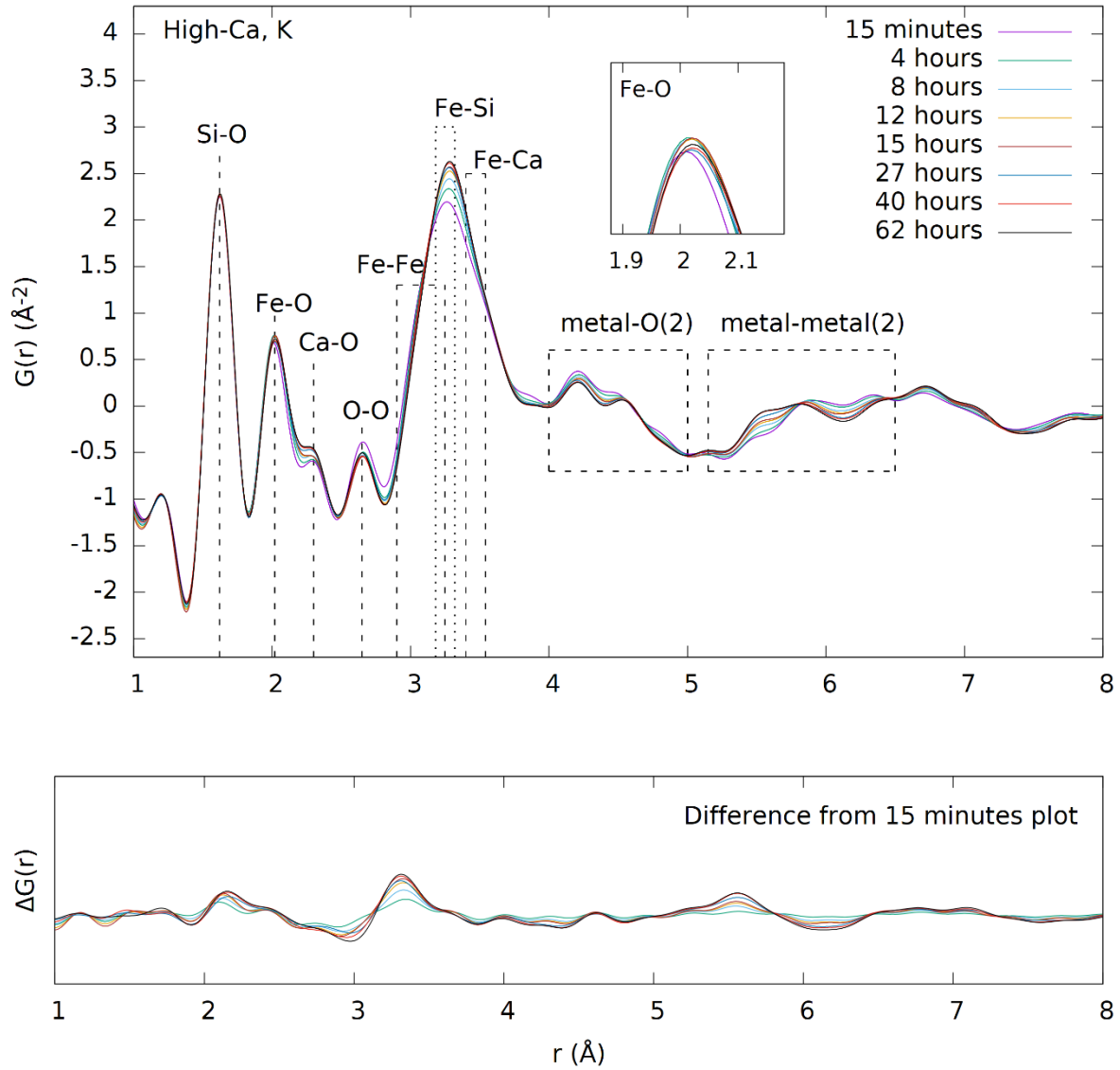


Figure 7: X-ray PDFs of the K-silicate activated high-Ca slag during the initial 62 hours of reaction.

Upper plot: Full PDFs and insert showing a zoom of the Fe-O correlation. Lower plot: Difference curves obtained by subtracting the initial data set (15 minutes) from those at later times.

The extensive changes seen in the PDFs in Figures 4 to 7 during the *in-situ* test are also observed at higher r values ($\sim 8 - 20$ Å; see Figures 8 and 9), especially for the Na-activated low-Ca slag system (Figure 8). For this sample, peaks emerge that are associated with the second (~ 5.6 Å) and third metal-metal correlations (~ 8.6 Å) [40]. Similar to the first metal-metal correlations (Figures 4 through 7), the changes as the reaction proceeds are less evident in the Na-activated high-Ca system, shown in Figure 9.

Assignment of the peaks associated with the second and third metal-metal correlations has been carried out using the simulated **partial** X-ray PDFs of mineral phases that are similar to the chemical composition of the various AAMs, as shown in Figure 10. The 15 minutes after mixing PDF for Na-activated low-Ca slag clearly aligns with the Fe-Fe(2) correlations in ferrosilite, the mineral phase closest in chemical composition (FeSiO_3) to the low-Ca slag. This, together with the fact that the first metal-metal peak is dominated by the Fe-Si correlation (as outlined above), implies that the bonding network for the low-Ca slag consists of Fe-O-Si-O-Fe linkages. Although it would be present in the slag, the Si-Si(2) is not observed in the PDF because of its relatively small scattering strength compared with Fe, and therefore has not been included in Figure 10.

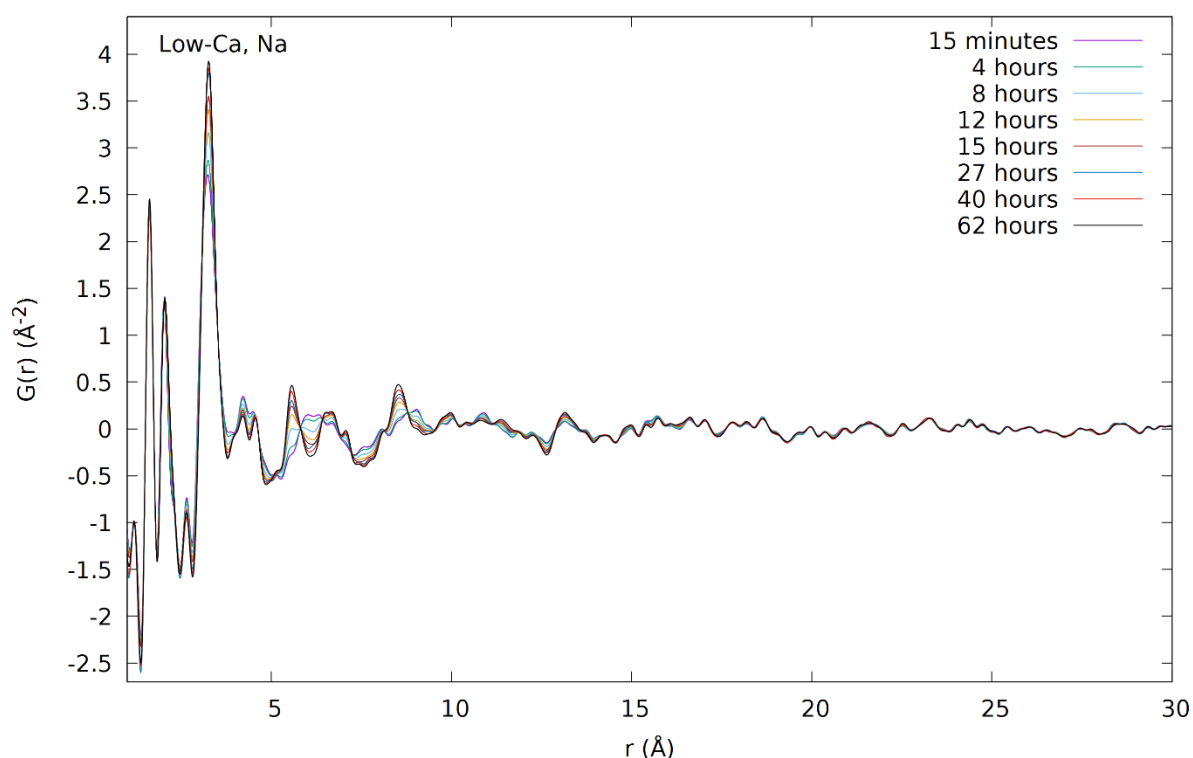


Figure 8: Long range X-ray PDFs of the Na-silicate activated low-Ca slag during the initial 62 hours of reaction.

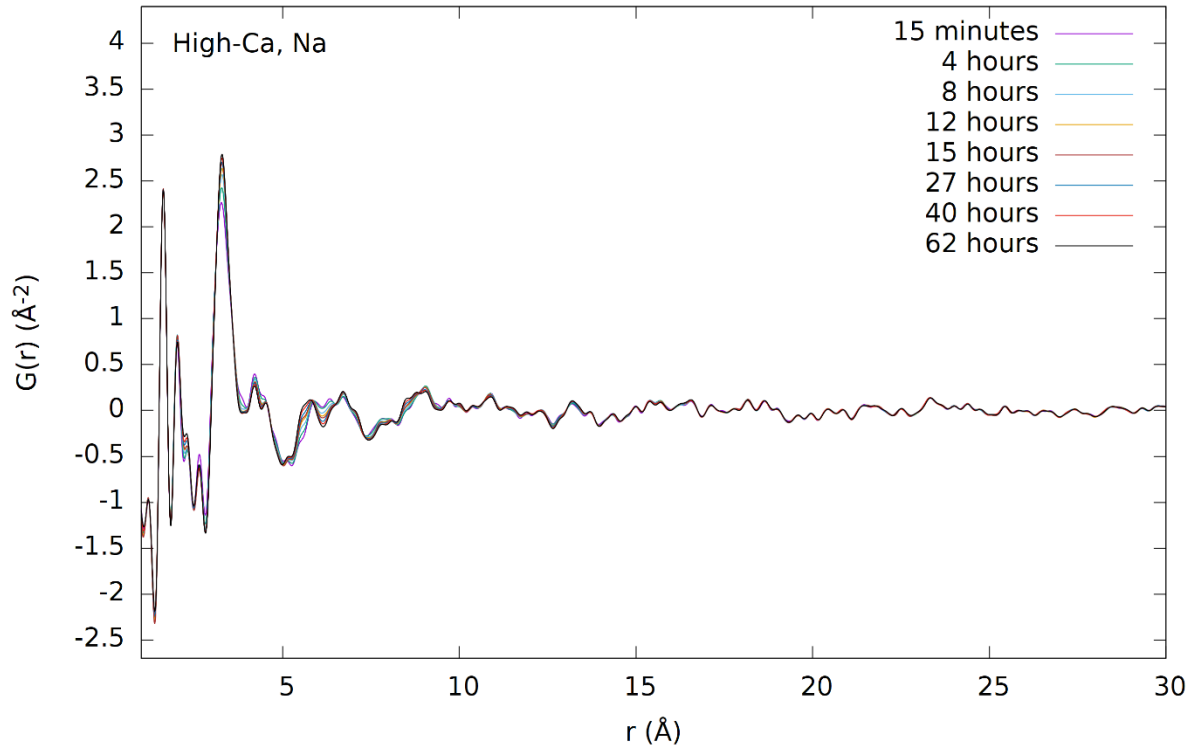


Figure 9: Long range X-ray PDFs of the Na-silicate activated high-Ca slag during the initial 62 hours of reaction.

During formation of the binder a clear rise in intensity is observed at 5.6 and 8.6 Å in the PDF data (Figure 8). As shown in Figure 10, these peaks correspond to the Fe-Fe distances in a trioctahedral layer (e.g., amakinite, $\text{Fe}(\text{OH})_2$). The peak at 5.6 Å also corresponds well to goethite, $\text{FeO}(\text{OH})$, but the agreement of the other correlations with the experimental data is less secure and the increased intensity should probably be associated with the observed increase of $^{\text{VI}}\text{Fe}^{2+}\text{-O-}^{\text{VI}}\text{Fe}^{2+}$ linkages, while goethite contains Fe^{3+} . Furthermore, there is a slight increase in the correlation at 6.5 Å, which distinguishes the trioctahedral layers from dioctahedral layers [57,58]. Importantly, for $\text{Fe}(\text{OH})_2$ shown in Figure 10, the correlations positioned at 5.6 Å and 8.6 Å are valid for any material containing layers of $^{\text{VI}}\text{Fe}^{2+}$ in trioctahedral configuration (as shown in Figure 11), provided that there is an Fe-Fe distance of 3.25 Å. There are peaks associated with $\text{Fe}(\text{OH})_2$ that do not appear in the experimental PDFs, specifically at 7.2 Å and 8.0 Å. These correlations correspond to out-of-plane distances in amakinite, and therefore the $^{\text{VI}}\text{Fe}^{2+}$ -containing layers are not stacked as would be expected for such an $\text{Fe}(\text{OH})_2$ phase. Instead, the PDF data indicate that the $^{\text{VI}}\text{Fe}^{2+}$ -containing phase may consist of alternating layers of trioctahedral

Fe(II)oxide and silicate. This proposed atomic arrangement is more closely related to mica or smectite clays, in which trioctahedral layers of network modifiers (usually Mg, intermixed with Fe or Ca) are stacked with layers of network-forming elements (Si, Al) [59-61]. There are also similarities between this stacking arrangement and that of calcium-silicate-hydrate (C-S-H) gel, in which calcium oxide sheets are sandwiched between layers consisting of silicate chains [62,63]. Alkali-activated blast furnace slags give rise to a similar structure, with the Al from the slag in tetrahedral positions, making it a C-A-S-H gel [24,54]. In cement nomenclature, the presented material might then be referred to as F-F-S-H or F²-S-H, as the Fe²⁺-trioctahedral clusters have similarities to the calcium oxide sheets, while the Fe³⁺ might have the same role in the silicate network as Al³⁺. No evidence of the layered nature of the silica was found in the PDF data, however, and the presence of silicate hydrates cannot be confirmed from the present experiments. Future work, including, for instance, inelastic neutron scattering [64], should clarify the role of H, in the form of OH and/or H₂O, in the structure of the alkali-activated Fe-rich slag.

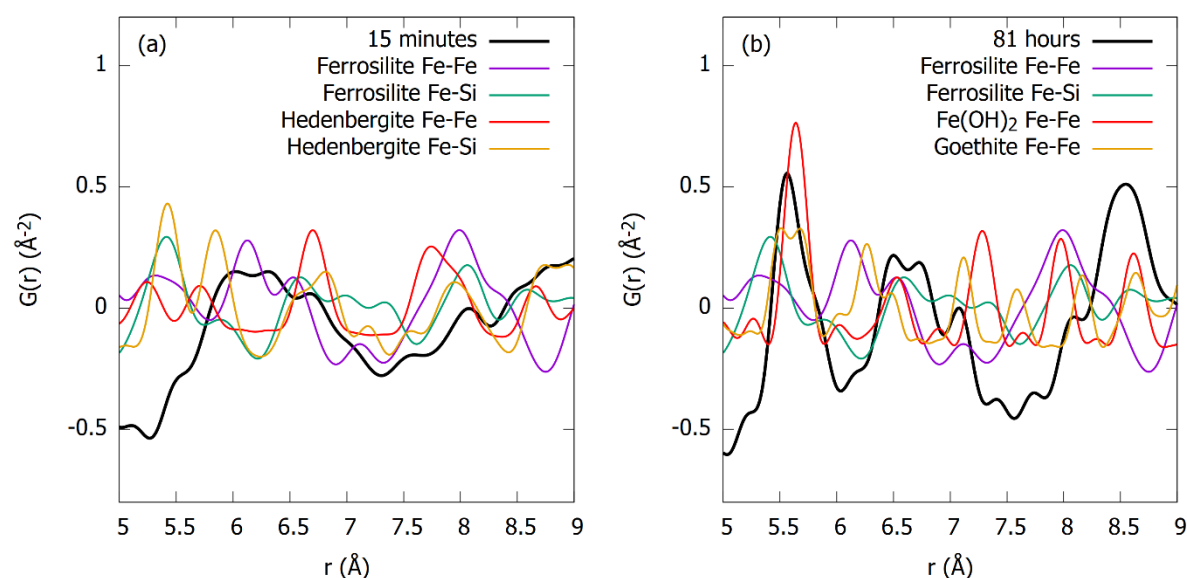


Figure 10: X-ray PDFs of (a) initial (15 minutes) and (b) final (81 hours) sample of the Na-activated low-Ca slag during the *in-situ* test, compared with ferrosilite ($\text{Fe}_2\text{Si}_2\text{O}_6$), hedenbergite ($\text{CaFeSi}_2\text{O}_6$), amakinite ($\text{Fe}(\text{OH})_2$) and goethite ($\text{FeO}(\text{OH})$).

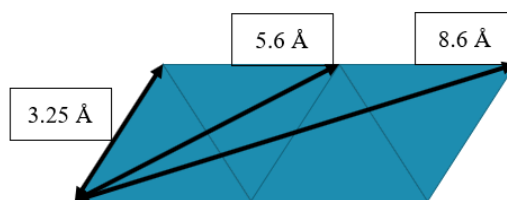


Figure 11: Calculation of the Fe-Fe distances in a trioctahedral Fe^{2+} layer. Fe atoms are located at the corners of the triangles.

With respect to the possibility of the formation of $\text{Fe}(\text{OH})_2$, it is known that high pH conditions are necessary for the precipitation of Fe-hydroxides [65]. Hence, the activating solutions, where the pH is ~ 13 -14, are ideal conditions for the formation of VIFe^{2+} -containing trioctahedral layers. Furthermore, the presence of silicates in solution will influence the precipitated products. For instance, hydrothermal synthesis from Fe-silicate solutions results in the precipitation of Fe-based layered double hydroxides (LDHs) or Fe-bearing clays [59,60,66-68]. Smectite or mica are examples of such clays [59-61] incorporating trioctahedral VIFe^{2+} layers. In the natural environment, Fe atoms within the trioctahedral layers are extensively intermixed with Ca and/or Mg [59-61].

In the alkali-activated high-Ca slag systems, the 5.6 Å and 8.6 Å peaks (associated with the Fe-Fe distances) show less increase compared with the low-Ca systems, even after taking into account the lower Fe content of the slag. This behavior indicates a lower extent of formation of the trioctahedral layer-containing phase in the high-Ca systems compared with low-Ca. There are two possible explanations for this behavior, the first being the intermixing of Ca atoms in the trioctahedral layers. Due to the larger ionic radius of Ca compared with Fe, this would lead to a distortion of the Fe-Fe distances associated with the trioctahedral layer and therefore broaden the corresponding peaks in the PDFs. The second explanation involves the Ca atoms preventing the formation of the VIFe^{2+} -trioctahedral layers. Assessment of the peak widths in Figures 8 and 9 reveals that limited peak broadening occurs in the high-Ca sample, and therefore the Ca atoms are disrupting the overall formation of the VIFe^{2+} -trioctahedral layers.

Additional information on the trioctahedral layer-containing phase can be obtained from the SAS region in Figures 1 to 3. The trioctahedral layer-containing phase (e.g., $\text{Fe}(\text{OH})_2$, LDH or clays) should show a

distinct peak in the SAS region representative of the basal spacing. As seen in Figure 3, the low-Ca systems undergo a more dramatic increase in SAS intensity compared with the high-Ca systems, which correlate with the intensity increase of the 5.6 and 8.6 Å peaks in the PDF. Although it is impossible in the present study to definitively determine if the SAS intensity is due to a basal spacing arising from the $^{VI}\text{Fe}^{2+}$ -containing phase or small pores, it is possible to state that the longer-term decrease in SAS intensity (Figure 2) is directly linked with the same decrease in intensity of 5.6 and 8.6 Å PDF correlations (see Figure 12). The evolution of the intensity of the SAS and the peak at 5.6 Å in the PDF is quantitatively compared in Figure 13. The rise and fall of both intensities show the same relation across different samples, suggesting that this SAS region is directly related to the $^{VI}\text{Fe}^{2+}$ -containing phase and shows that, after extensive curing, the $^{VI}\text{Fe}^{2+}$ -containing phase has undergone significant alterations, as discussed in the next section.

As seen in Figure 8, the ordering of the $^{VI}\text{Fe}^{2+}$ trioctahedral layer only extends up to ~9 Å. Hence, the domain size for these ordered layers corresponds to approximately 20 FeO_6 units. The formation of these $^{VI}\text{Fe}^{2+}$ domains can explain previous results from Fourier-transform infrared spectroscopy [37,69], where a shift of the Si-O stretching band to higher wavenumbers (from 850-900 to ~950 cm^{-1}) was observed as the slag dissolves and binder forms. The $^{VI}\text{Fe}^{2+}$ clustering and associated decrease in the Fe-Si correlation and increase in Fe-Fe causes an increase in the Si-Si correlation, when assuming that the connectivity of the Si units remains relatively unchanged. The amount of Si-O-Si bonds is thereby increased (the amount of non-bridging oxygens is decreased), and the wavenumber of the Si-O stretching band increases. These Si-Si correlations are not clearly observed in the current PDF study because of the low scattering strength of Si with respect to Fe. In terms of nanoscale ordering of the AAM paste, the main phase that contributes to an increase in ordering with respect to the initial slag is the $^{VI}\text{Fe}^{2+}$ -containing trioctahedral structure, where the remainder of the material does not contribute to intermediate range ordering (Figures 8 and 9) and therefore the $^{IV}\text{Fe}^{3+}$ -containing silicate network is amorphous.

The atomic rearrangements seen in Figures 4 through 7 for the *in-situ* reactions have been compared with the extensively cured and milled pastes in previous work, where the same pastes as reported in

Peys et al. [40] were measured again at ~6 months after mixing. Figure 12 compares the *in-situ* Na-activated low-Ca sample after 62 hours of reaction with the 6 months cured version (61 days closed bottle, total age ~6 months), where a clear shift of the Fe-O correlation to a lower distance can be observed. This behavior is associated with the change in oxidation state of Fe, where the initially formed $^{VI}\text{Fe}^{2+}$ -species in the layered trioctahedral configuration (also observed in previous work [39]) transition to $^{IV}\text{Fe}^{3+}$. This transition is also noticeable in the metal-metal correlations via the decrease in intensity of the features associated to the trioctahedral layers. The intensity at 3.25 Å together with this peak's area are seen to decrease, indicating a transition from Fe-Fe linkages to Fe-Si. This transition is accompanied by a decrease in intensity of the peaks at 5.6 and 8.6 Å. It can be concluded, therefore, that the trioctahedral layers are converted when the Fe^{2+} species undergo oxidation during the later stages of reaction or during the milling procedure described in previous work [40]. During this oxidation, no change in color is observed, the samples remain dark grey. This indicates that the formed Fe^{3+} is not present as hematite, which would turn the samples red/brown, but a phase with a more dark or less intense color. Future studies should concentrate on the later stage process(es) to determine the exact cause of the oxidation reaction and influence on macroscopic properties. Furthermore, as seen in Figure 12 for the 6 months sample, a peak is still observed at around 5.6 Å (also at 8.6 Å), indicating that a residue of the trioctahedral layers remains within the material.

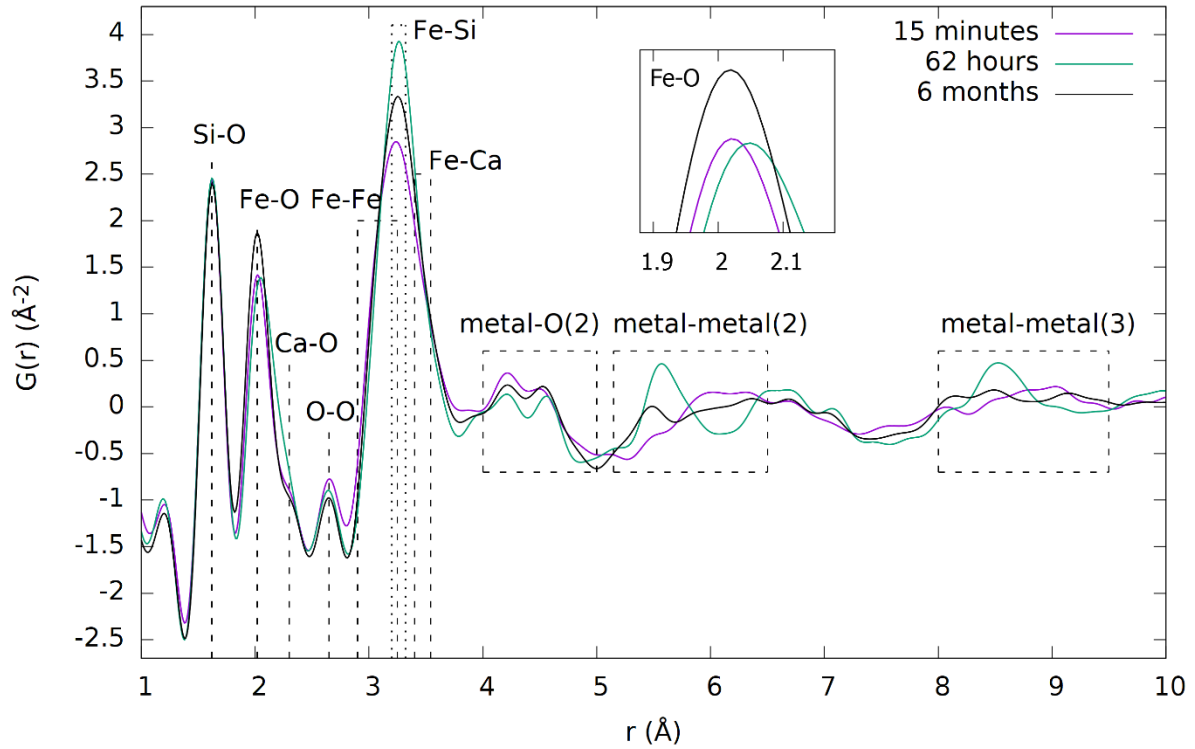


Figure 12: Comparison of the X-ray PDFs of the Na-activated low-Ca slag immediately after mixing (15 minutes), after 62 hours of reaction and extensively cured/oxidized from previous work [40]. The insert shows a zoom of the Fe-O correlation.

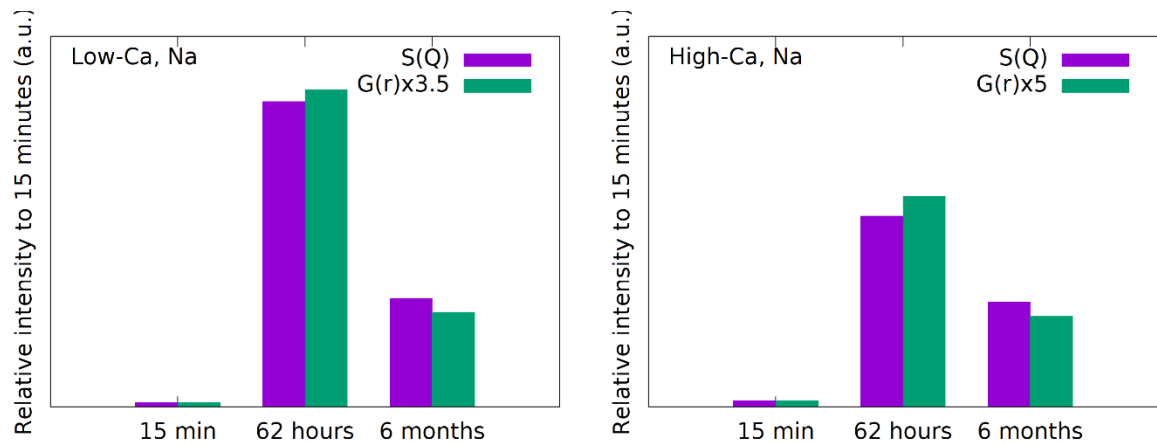


Figure 13: Comparison between the intensity of the SAS and peak at 5.6 Å in the PDF for the low-Ca (left) and high-Ca (right) system for the same times as presented in Figure 12. Note that the units for the scattering function and PDF are intensity (arb. units) and Å⁻², respectively.

The reaction kinetics have been evaluated using the atom-atom correlations that showed the biggest change during the *in-situ* measurements, specifically the intensity 5.57 \AA . As seen in Figure 14a, the intensity of the 5.57 \AA correlation shows a similar trend as the SAS intensity in Figure 3. An induction period for the reactions that form the binder is observed at the beginning of the reaction (initial 2-3 hours), after which the reaction rate increases. This is contrary to the *in-situ* changes seen in metakaolin-based AAMs, where no induction periods were identified [21]. To determine the rate law of the reactions, the data are plotted in Figure 14 on linear, logarithmic and reciprocal axes. Two straight lines are observed in Figure 14c and the overall formation reaction therefore follows a logarithmic rate law indicative of two separate pseudo-single step first-order rate expressions, corresponding to the dissolution-dominated and polymerization-dominated stages.

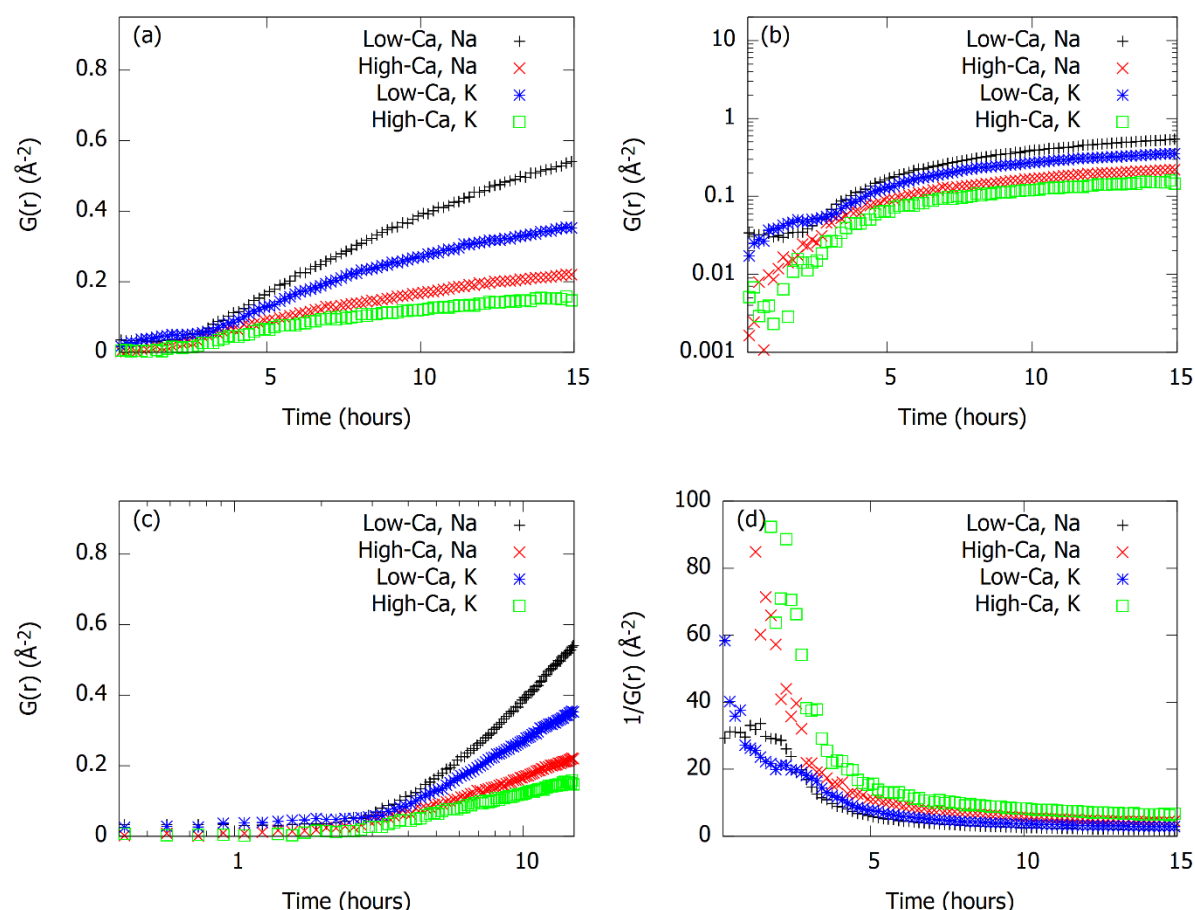


Figure 14: Evolution of the intensity of the 5.57 \AA correlation in the X-ray PDFs on a (a) linear scale; G , (b) logarithmic y-axis; log time, (c) logarithmic x-axis; log G , (d) reciprocal y-axis; $1/G$.

The PDF curves during the dormant period are shown in Figure 15 for the K-activated and Na-activated low-Ca samples over an r range of $1.4 \leq r \leq 4.0$. While previous work involving Mössbauer spectroscopy [39] showed that the oxidation state and coordination number of Fe stays constant during this period ($\sim 90\%$ Fe^{2+} ; combination of 4- and 5-fold coordinated species), it is also clear from Figure 15 that the Na-system only starts to show changes after ~ 3 hours (also seen for this sample in Figure 4), whereas the K-system shows subtle changes to the local atomic structure immediately after mixing. In particular, the Fe-O correlation is seen to increase in both intensity and distance, which indicates an increase in the average coordination number of Fe towards 5. An increase in 5-fold coordinated Fe, rather than a combination of 4- and 5-fold, results in the increase in intensity of the Fe-O correlation, as more Fe-O bonds are present in the system. In addition to the changes seen in the Fe-O correlation in Figure 15, the rearrangements are also seen as a rise in intensity at ~ 3.25 Å and decline at ~ 2.8 Å. These changes indicate a reconfiguration in the metal-metal correlations, as a consequence of the increased coordination number of Fe and can be influenced by a change in the K-O correlation, which should also be present at ~ 2.8 Å. The lack of rearrangements in the Na-system before the polymerization reactions (~ 3 hours after mixing) indicates that the dissolution of the slag liberates Fe-silicate clusters, i.e., the slag is not dissolved to the ionic level, where the Fe atoms retain their original coordination environment found in the slag. In the K-system, the Fe coordination of these clusters in solution change during the induction period, as described above. The kinetics of the changes of the Fe-O correlations are presented in Figure 16. After the rapid intensity increase of the Fe-O correlation for the K-system, the intensity of this correlation slowly declines again. This decline is also observed in the Na-system and can be explained by the formation of the $^{\text{VI}}\text{Fe}^{2+}$ -trioctahedral clusters. The rise of the $^{\text{VI}}\text{Fe}^{2+}$ -O correlation at 2.14 Å at the expense of 4- and 5-fold coordinated Fe^{2+} (1.99 - 2.06 Å) results in a broadening of the Fe-O correlation. Hence, the reaction mechanism of Fe-rich AAMs can be summarized as follows:

1. Dissolution of precursor; liberating Fe-silicate species with the same atomic arrangement as the slag (for Na), or a similar atomic arrangement but with an increased coordination number of Fe (for K).

2. After reaching a threshold value of Fe-silicate species in solution, the simultaneous formation of $^{VI}\text{Fe}^{2+}$ trioctahedral layers and a $^{IV}\text{Fe}^{3+}$ -incorporating silicate binder phase with an increased degree of polymerization with respect to the precursor.
3. The oxidation of the $^{VI}\text{Fe}^{2+}$ trioctahedral layers towards more Fe^{3+} binder.

These reaction stages are schematically presented in Figure 17, which is an updated and more detailed version of a figure from previous work [39].

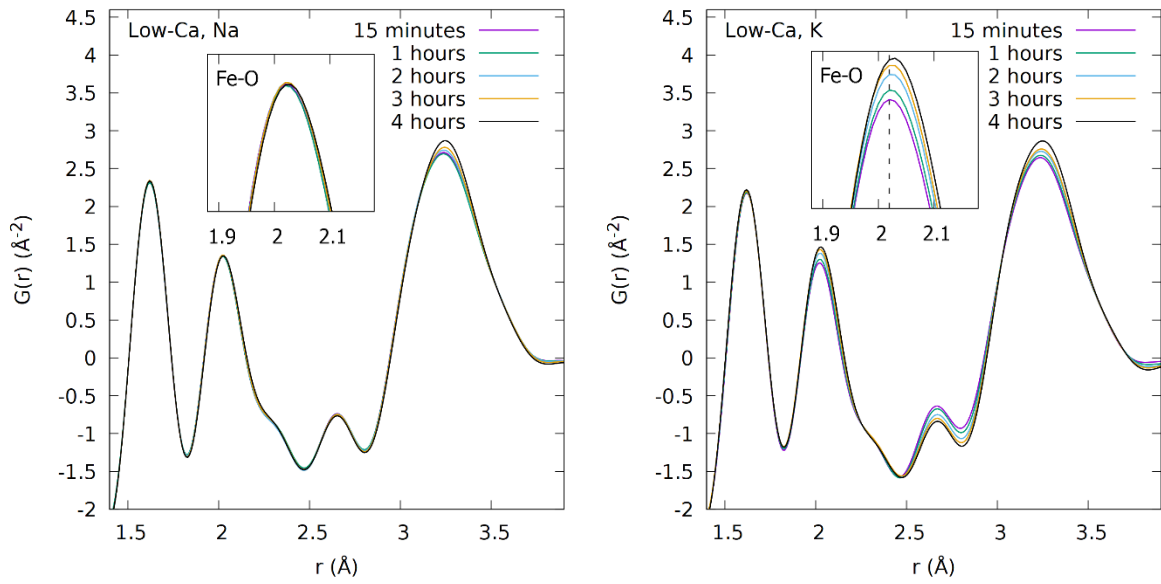


Figure 15: Low r region of the X-ray PDFs for the low-Ca AAMs during the first 4 hours. The insert shows a zoom of the nearest neighbor Fe-O correlation.

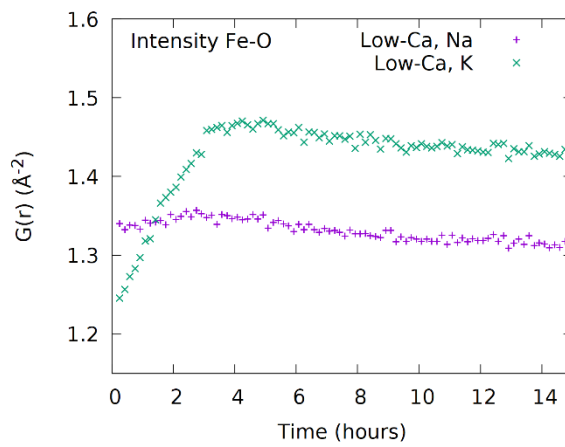


Figure 16: Evolution of the intensity for the nearest neighbor Fe-O correlation in the low-Ca systems.

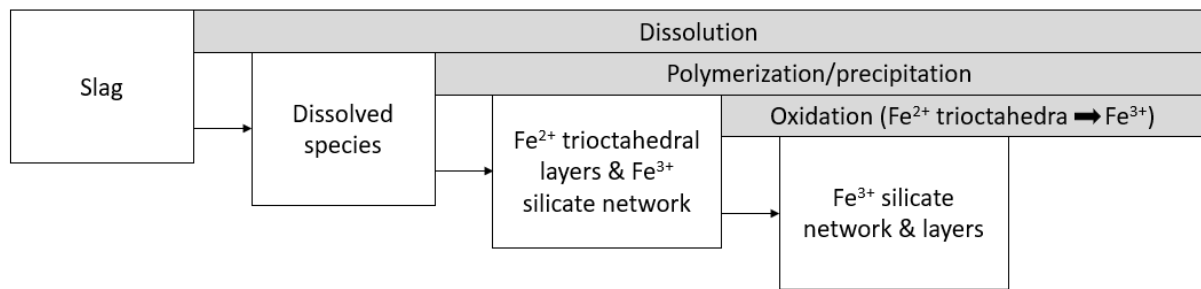


Figure 17: Schematic overview of the formation mechanism and different reaction stages of alkali-activated Fe-rich slag.

This reaction mechanism, and the unique last step (i.e., late stage oxidation) in particular, can have repercussions for the macroscopic behavior of the Fe-rich AAMs. The oxidation reactions may lead to a volume reduction (i.e., shrinkage). To accurately quantify this potential shrinkage, detailed atomistic representations or molar volumes would be required for the $^{\text{VI}}\text{Fe}^{2+}$ -containing structure and the $^{\text{IV}}\text{Fe}^{3+}$ -containing silicate binder phase, as changes in coordination can result in geometrical shrinkage/expansion that cannot be determined solely using bond length changes. Moreover, it is unclear how rapidly this oxidation step would occur for non-milled samples, as exposure to an oxidizing environment for solid samples would depend on the diffusion rate of gas molecules through the partially-saturated pore network, which in turn would control the level of shrinkage attained during the life-time of the concrete. It is interesting to note that a decrease in the mechanical properties of the Fe-rich AAMs has not been observed to date [30,70]. Future research concentrating on shrinkage data and pore structure information is needed, therefore, to enable more accurate prediction of the long-term performance of these novel Fe-rich binders.

Conclusions

The formation of low- CO_2 AAMs starting from $\text{CaO-FeO}_x\text{-SiO}_2$ slag as the precursor was studied using *in-situ* X-ray total scattering and PDF analysis. Two slags with molar composition $0.83\text{FeO-SiO}_2\text{-}0.17\text{CaO}$ and $0.67\text{FeO-SiO}_2\text{-}0.33\text{CaO}$ were mixed with sodium and potassium silicate solutions. Three reaction stages were identified from the *in-situ* measurements: dissolution, polymerization and oxidation. During the initial few hours, the reactions are dominated by dissolution of the Fe-rich slag,

and the atomic rearrangements of the Fe-silicate species released into solution depend on the alkali cation. For sodium, the atomic correlations of the intermediate species in solution are found to be exactly the same as those in the precursor slag. In contrast, potassium causes an increase in the coordination number of Fe once it is released into solution. The setting of the binder commences with the formation of two new phases with different Fe oxidation states (i.e., the polymerization stage). The Fe^{3+} -containing silicate network did not explicitly reveal details of its structure in the PDFs, apart from its glassy nature. The total scattering and PDF data do reveal the emergence of $^{\text{VI}}\text{Fe}^{2+}$ trioctahedral layers, however, especially for the low-Ca slag AAMs. The Fe-O distance associated with this phase is positioned at 2.14 Å, resulting in higher *r* Fe-Fe distances at 3.25, 5.6 and 8.6 Å. These $^{\text{VI}}\text{Fe}^{2+}$ -containing layers are characteristic of $\text{Fe}(\text{OH})_2$ and layered double hydroxides (LDHs) and observed in nature in clay minerals, e.g. in smectites or micas. The kinetics of formation of these layers follow a logarithmic rate law. A comparison with well-developed milled samples (> 6 months) suggests that the Fe associated with the trioctahedral layers undergoes oxidation over the long term. Hence, this investigation has discovered the formation mechanism of Fe-rich alkali-activated binders, enabling future studies to focus on the processing and performance of these materials by manipulating the fundamental formation behavior and the long-term performance of the material under the influence of the observed oxidation reaction.

Acknowledgments

Arne Peys is thankful to the Research Foundation – Flanders (FWO) for the PhD scholarship and additional funding for international mobility. Participation of Claire E. White in this project was enabled by the National Science Foundation under Grant No. 1362039. Use of the Advanced Photon Source, an Office of Science User Facility operated for the U.S. Department of Energy (DOE) Office of Science by Argonne National Laboratory, was supported by the U.S. DOE under Contract No. DE-AC02-06CH11357. The authors would like to thank Olaf Borkiewicz, Karena Chapman, Kevin Beyer and Rick Spence from Argonne National Laboratory and Kengran Yang and Kai Gong from Princeton University for support during the experiments at the Advanced Photon Source.

References

- [1] A. Nazari, J. G. Sanjayan, Handbook of Low-Carbon Concrete, Elsevier, Oxford, UK, 2017.
- [2] F. Pacheco-Torgal, S. Jalali, J. Labrincha, V. M. John, Eco-Efficient Concrete, Woodhead Publishing, Cambridge, UK, 2013.
- [3] P. J. M. Monteiro, S. A. Miller, A. Horvath, Towards sustainable concrete, *Nat. Mater.* 16 (2017) 698-699. <https://doi.org/10.1038/nmat4930>.
- [4] S. Jewell, S. M. Kimball, Minerals Commodity Summaries, Report for the U.S. Department of the Interior and the U.S. Geological Survey, 2014.
- [5] J. L. Provis, J. S. J. van Deventer, Alkali Activated Materials: State-of-the-Art Report RILEM TC 224-AAM, Springer, Dordrecht Heidelberg New York London, 2014.
- [6] J. S. J. van Deventer, J. L. Provis, P. Duxson, Technical and commercial progress in the adoption of geopolymer cement, *Miner. Eng.* 29 (2012) 89-104. <https://doi.org/10.1016/j.mineng.2011.09.009>.
- [7] J. S. J. van Deventer, Progress in the Adoption of Geopolymer Cement, in: A. Nazari, J. G. Sanjayan (Eds.), Handbook of Low-Carbon Concrete, Elsevier, Oxford, UK, 2017, pp. 217-262.
- [8] J. Davidovits, Geopolymers: Inorganic polymeric new materials, *J. Therm. Anal.* 37 (1991) 1633-1656. <https://doi.org/10.1007/BF01912193>.
- [9] H. Rahier, B. Van Mele, M. Biesemans, J. Wastiels, X. Wu, Low-temperature synthesized aluminosilicate glasses, Part I: Low-temperature reaction stoichiometry and structure of a model compound, *J. Mater. Sci.* 31 (1996) 71-79. <https://doi.org/10.1007/BF00355128>.
- [10] H. Rahier, J. Wastiels, M. Biesemans, R. Willem, G. Van Assche, B. Van Mele, Reaction mechanism, kinetics and high temperature transformations of geopolymers, *J. Mater. Sci.* 42 (2007) 2982-2996. <https://doi.org/10.1007/s10853-006-0568-8>.
- [11] P. Duxson, A. Fernandez-Jimenez, J. L. Provis, G. C. Lukey, A. Palomo, J. S. J. van Deventer, Geopolymer technology: the current state of the art, *J. Mater. Sci.* 42 (2007) 2917-2933. <https://doi.org/10.1007/s10853-006-0637-z>.

- [12] K. Yang, C. E. White, Modeling the Formation of Alkali Aluminosilicate Gels at the Mesoscale Using Coarse-Grained Monte Carlo, *Langmuir* 32 (2016) 11580-11590.
<https://doi.org/10.1021/acs.langmuir.6b02592>.
- [13] J. L. Provis, J. S. J. van Deventer, Geopolymerisation kinetics. 2. Reaction kinetic modelling, *Chem. Eng. Sci.* 62 (2007) 2318-2329. <https://doi.org/10.1016/j.ces.2007.01.028>.
- [14] A. Hajimohammadi, J. L. Provis, J. S. J. van Deventer, Effect of Alumina Release Rate on the Mechanism of Geopolymer Gel Formation, *Chem. Mater.* 22 (2010) 5199-5208.
<https://doi.org/10.1021/cm101151n>.
- [15] A. Gharzouni, E. Joussein, B. Samet, S. Baklouti, S. Rossignol, Effect of the reactivity of alkaline solution and metakaolin on geopolymer formation, *J. Non-Cryst. Solids* 410 (2015) 127-134.
<https://doi.org/10.1016/j.jnoncrysol.2014.12.021>.
- [16] Y. Pontikes, L. Machiels, S. Onisei, L. Pandelaers, D. Geysen, P. T. Jones, B. Blanpain, Slags with a high Al and Fe content as precursors for inorganic polymers, *Appl. Clay Sci.* 73 (2013) 93-102.
<https://doi.org/10.1016/j.clay.2012.09.020>.
- [17] H. Rahier, W. Simons, B. Van Mele, M. Biesemans, Low-temperature synthesized aluminosilicate glasses, Part III: Influence of the composition of the silicate solution on production, structure and properties, *J. Mater. Sci.* 32 (1997) 2237-2247. <https://doi.org/10.1023/A:1018563914630>.
- [18] S. Onisei, K. Lesage, B. Blanpain, Y. Pontikes, Early Age Microstructural Transformations of an Inorganic Polymer Made of Fayalite Slag, *J. Am. Ceram. Soc.* 98 (2015) 2269-2277.
<https://doi.org/10.1111/jace.13548>.
- [19] H. Rahier, J. F. Denayer, B. Van Mele, Low-temperature synthesized aluminosilicate glasses, Part IV: Modulated DSC study on the effect of particle size of metakaolinite on the production of inorganic polymer glasses, *J. Mater. Sci.* 38 (2003) 3131-3136. <https://doi.org/10.1023/A:1024733431657>.

- [20] C. E. White, K. Page, N. J. Henson, J. L. Provis, In situ synchrotron X-ray pair distribution function analysis of the early stages of gel formation in metakaolin-based geopolymers, *Appl. Clay Sci.* 73 (2013) 17-25. <https://doi.org/10.1016/j.clay.2012.09.009>.
- [21] C. E. White, J. L. Provis, B. Bloomer, N. J. Henson, K. Page, In situ X-ray pair distribution function analysis of geopolymer gel nanostructure formation kinetics, *Phys. Chem. Chem. Phys.* 15 (2013) 8573-8582. <https://doi.org/10.1039/c3cp44342f>.
- [22] C. A. Rees, J. L. Provis, G. C. Lukey, J. S. J. van Deventer, In Situ ATR-FTIR Study on the Early Stages of Fly Ash Geopolymer Gel Formation, *Langmuir* 23 (2007) 9076-9082. <https://doi.org/10.1021/la701185g>.
- [23] C. E. White, J. L. Provis, T. Proffen, J. S. J. van Deventer, Molecular mechanisms responsible for the structural changes occurring during geopolymerization: Multiscale simulation, *AIChE J.* 58 (2012) 2241-2253. <https://doi.org/10.1002/aic.12743>.
- [24] J. L. Provis, A. Palomo, C. Shi, Advances in understanding alkali-activated materials, *Cement Concrete Res.* 78 (2015) 110-125. <https://doi.org/10.1016/j.cemconres.2015.04.013>.
- [25] C. E. White, J. L. Provis, A. Llobet, T. Proffen, J. S. J. van Deventer, Evolution of Local Structure in Geopolymer Gels: An In Situ Neutron Pair Distribution Function Analysis, *J. Am. Ceram. Soc.* 94 (2011) 3532-3539. <https://doi.org/10.1111/j.1551-2916.2011.04515.x>.
- [26] P. L. Lopez Gonzalez, R. M. Novais, J. A. Labrincha, B. Blanpain, Y. Pontikes, Modifications of basic-oxygen-furnace slag microstructure and their effect on the rheology and the strength of alkali-activated binders, *Cement Concrete Comp.* 97 (2019) 143-153. <https://doi.org/10.1016/j.cemconcomp.2018.12.013>.
- [27] T. Hertel, B. Blanpain, Y. Pontikes, A proposal for a 100% use of bauxite residue towards inorganic polymer mortar, *J. Sustain. Metall.* 2 (2016) 394-404. <https://doi.org/10.1007/s40831-016-0080-6>.

- [28] K. Komnitsas, D. Zaharaki, V. Perdikatsis, Geopolymerisation of low-Calcium ferronickel slags, *J. Mater. Sci.* 42 (2007) 3073-3082. <https://doi.org/10.1007/s10853-006-0529-2>.
- [29] S. Onisei, Y. Pontikes, T. Van Gerven, G. N. Angelopoulos, T. Velea, V. Predica, P. Moldovan, Synthesis of inorganic polymers using fly ash and primary lead slag, *J. Hazard. Mater.* 205-206 (2012) 101-110. <https://doi.org/10.1016/j.jhazmat.2011.12.039>.
- [30] L. Kriskova, L. Machiels, Y. Pontikes, Inorganic Polymers from a Plasma Converter Slag: Effect of Activating Solution on Microstructure and Properties, *Journal of Sustainable Metallurgy* 1 (2015) 240-251. <https://doi.org/10.1007/s40831-015-0022-8>.
- [31] E. Kamseu, I. Lancellotti, V. M. Sglavo, L. Modolo, C. Leonelli, Design of Inorganic Polymer Mortar from Ferric silicic and Calsialic Slags for Indoor Humidity Control, *Materials* 9 (2016) 410-427. <https://doi.org/10.3390/ma9060410>.
- [32] R. I. Iacobescu, V. Cappuyens, T. Geens, L. Kriskova, S. Onisei, P. T. Jones, Y. Pontikes, The influence of curing conditions on the mechanical properties and leaching of inorganic polymers made of fayalitic slag, *Front. Chem. Sci. Eng.* 11 (2017) 317-327. <https://doi.org/10.1007/s11705-017-1622-6>.
- [33] A. Peys, L. Arnout, B. Blanpain, H. Rahier, K. Van Acker, Y. Pontikes, Mix-Design Parameters and Real-Life Considerations in the Pursuit of Lower Environmental Impact Inorganic Polymers, *Waste Biomass Valori.* 9 (2018) 879-889. <https://doi.org/10.1007/s12649-017-9877-1>.
- [34] G. Habert, C. Ouellet-Plamondon, Recent update on the environmental impact of geopolymers, *RILEM Tech. Lett.* 1 (2016) 17-23. <https://doi.org/10.21809/rilemtechlett.2016.6>.
- [35] P. N. Lemougna, K. J. D. MacKenzie, G. N. L. Jameson, H. Rahier, U. F. Chinje Melo, The role of iron in the formation of inorganic polymers (geopolymers) from volcanic ash: a ^{57}Fe Mössbauer spectroscopy study, *J. Mater. Sci.* 48 (2013) 5280-5286. <https://doi.org/10.1007/s10853-013-7319-4>.
- [36] L. Arnout, A. Peys, L. Machiels, P. T. Jones, S. Arnout, E. Nagels, B. Blanpain, Y. Pontikes, unpublished work.

- [37] S. Onisei, A. P. Douvalis, A. Malfliet, A. Peys, Y. Pontikes, Inorganic Polymers Made of Fayalite Slag: Effect of Activating Solution and Curing on the Microstructure and behaviour of Fe, *J. Am. Ceram. Soc.* 101 (2018) 2245-2257. <https://doi.org/10.1111/jace.15420>.
- [38] S. Simon, G. Gluth, A. Peys, S. Onisei, D. Banerjee, Y. Pontikes, The Fate of Iron During the Alkali-Activation of Synthetic $\text{FeO}_x\text{-SiO}_2\text{-(CaO)}$ Slags: an Fe K-edge XANES Study, *J. Am. Ceram. Soc.* 101 (2018) 2107-2118. <https://doi.org/10.1111/jace.15354>.
- [39] A. Peys, A. P. Douvalis, V. Hallet, H. Rahier, B. Blanpain, Y. Pontikes, Inorganic polymers from $\text{CaO-FeO}_x\text{-SiO}_2$ slag: the start of oxidation of Fe and the formation of a mixed valence binder, submitted.
- [40] A. Peys, C. E. White, D. Olds, H. Rahier, B. Blanpain, Y. Pontikes, Molecular structure of $\text{CaO-FeO}_x\text{-SiO}_2$ glassy slags and resultant inorganic polymers, *J. Am. Ceram. Soc.* 101 (2018) 5846-5857. <https://doi.org/10.1111/jace.15880>.
- [41] X. Qiu, J. W. Thompson, S. J. L. Billinge, PDFgetX2: a GUI-driven program to obtain the pair distribution function from X-ray powder diffraction data, *J. Appl. Crystallogr.* 37 (2004) 678. <https://doi.org/10.1107/S0021889804011744>.
- [42] C. L. Farrow, P. Juhas, D. Bryndin, E. S. Bozin, J. Bloch, T. Proffen, S. J. L. Billinge, PDFfit2D and PDFgui: computer programs for studying nanostructure in crystals, *J. Phys. Condens. Mat.* 19 (2007) 335219. <https://doi.org/10.1088/0953-8984/19/33/335219>.
- [43] P. Steins, A. Poulesquen, O. Diat, F. Frizon, Structural Evolution during Geopolymerization from an Early Age to Consolidated Material, *Langmuir* 28 (2012) 8502-8510. <https://doi.org/10.1021/la300868v>.
- [44] J. Melar, G. Renaudin, F. Leroux, A. Hardy-Dessources, J.-M. Nedelec, C. Taviot-Gueho, E. Petit, P. Steins, A. Poulesquen, F. Frizon, The Porous Network and its Interface inside Geopolymers as a Function of Alkali Cation and Aging, *J. Phys. Chem. C* 119 (2015) 17619-17632. <https://doi.org/10.1021/acs.jpcc.5b02340>.
- [45] R. P. Williams, A. van Riessen, The First 20 Hours of Geopolymerization: An in Situ WAXS Study of Fly ash-Based Geopolymers, *Materials* 9 (2016) 552-564. <https://doi.org/10.3390/ma9070552>.

- [46] S. Soyer-Uzun, S. R. Chae, C. J. Benmore, H.-R. Wenk, P. J. M. Monteiro, Compositional Evolution of Calcium Silicate Hydrate (C–S–H) Structures by Total X-Ray Scattering, *J. Am. Ceram. Soc.* 95 (2012) 793-798. <https://doi.org/10.1111/j.1551-2916.2011.04989.x>.
- [47] P. Steins, A. Poulesquen, F. Frizon, O. Diat, J. Jestin, J. Causse, D. Lambertin, S. Rossignol, Effect of aging and alkali activator on the porous structure of a geopolymer, *J. Appl. Crystallogr.* 47 (2014) 316-324. <https://doi.org/10.1107/S160057671303197X>.
- [48] C. Weigel, L. Cormier, G. Calas, L. Galois, D. T. Bowron, Intermediate-range order in the silicate network glasses $\text{NaFexAl}_{1-x}\text{Si}_2\text{O}_6$ ($x = 0, 0.5, 0.8, 1$): A neutron diffraction and empirical potential structure refinement modeling investigation, *Phys. Rev. B* 78 (2008) 064202. <https://doi.org/10.1103/PhysRevB.78.064202>.
- [49] J. L. Bell, P. Sarin, P. E. Driemeyer, R. P. Haggerty, P. J. Chupas, W. M. Kriven, X-ray pair distribution function analysis of a metakaolin-based, $\text{KAlSi}_2\text{O}_6 \cdot 5.5\text{H}_2\text{O}$ inorganic polymer (geopolymer), *J. Mater. Chem.* 48 (2008) 5974-5981. <https://doi.org/10.1039/B808157C>.
- [50] A. C. Wright, S. J. Clarke, C. K. Howard, P. A. Bingham, S. D. Forder, D. Holland, D. Martlew, H. E. Fischer, The environment of $\text{Fe}^{2+}/\text{Fe}^{3+}$ cations in a soda-lime-silica glass, *Physical Chemistry of Glasses: European Journal of Glass Science and Technology B* 55 (2014) 243-252.
- [51] N. N. Greenwood, T. C. Gibb, *Mössbauer Spectroscopy*, Chapman and Hall, London, UK, 1971.
- [52] C. E. White, Effects of temperature on the atomic structure of synthetic calcium-silicate-deuterate gels: A neutron pair distribution function investigation, *Cement Concrete Res.* 79 (2016) 93-100. <https://doi.org/10.1016/j.cemconres.2015.09.001>.
- [53] S. Rossano, A. Y. Ramos, J.-M. Delaye, Environment of ferrous iron in $\text{CaFeSi}_2\text{O}_6$ glass; contributions of EXAFS and molecular dynamics, *J. Non-Cryst. Solids* 273 (2000) 48-52. [https://doi.org/10.1016/S0022-3093\(00\)00124-1](https://doi.org/10.1016/S0022-3093(00)00124-1).
- [54] C. E. White, L. L. Daemen, M. Hartl, K. Page, Intrinsic differences in atomic ordering of calcium (alumino)silicate hydrates in conventional and alkali-activated cements, *Cement Concrete Res.* 67 (2015) 66-73. <https://doi.org/10.1016/j.cemconres.2014.08.006>.

- [55] A. E. Morandau, C. E. White, In situ X-ray pair distribution function analysis of accelerated carbonation of a synthetic calcium-silicate-hydrate gel, *J. Mater. Chem. A* 3 (2015) 8597-8605. <https://doi.org/10.1039/C5TA00348B>.
- [56] N. Garg, C. E. White, Mechanism of zinc oxide retardation in alkali-activated materials: an in situ X-ray pair distribution function investigation, *J. Mater. Chem. A* 5 (2017) 11794-11804. <https://doi.org/10.1039/C7TA00412E>.
- [57] S. I. Tzipursky, V. A. Drits, The distribution of octahedral cations in the 2:1 layers of dioctahedral smectites studied by oblique texture electron diffraction, *Clay Miner.* 19 (1984) 177-193. <https://doi.org/10.1180/claymin.1984.019.2.05>.
- [58] M. D. Foster, Layer charge relations in dioctahedral and trioctahedral micas, *Am. Mineral.* 45 (1960) 383-398.
- [59] E. Ferrow, Mössbauer Effect and X-ray Diffraction Studies of Synthetic Iron Bearing Trioctahedral Micas, *Phys. Chem. Miner.* 14 (1987) 276-280. <https://doi.org/10.1007/BF00307994>.
- [60] G. J. Redhammer, Characterisation of synthetic trioctahedral micas by Mössbauer spectroscopy, *Hyperfine Interact.* 117 (1998) 85-115. <https://doi.org/10.1023/A:1012639225782>.
- [61] C. A. Gorski, L. Klüpfel, A. Voegelin, M. Sander, T. B. Hofstetter, Redox Properties of Structural Fe in Clay Minerals. 2. Electrochemical and Spectroscopic Characterization of Electron Transfer Irreversibility in Ferruginous Smectite, SWa-1, *Environ. Sci. Technol.* 46 (2012) 9369-9377. <https://doi.org/10.1021/es302014u>.
- [62] H. F. W. Taylor, Proposed Structure for Calcium Silicate Hydrate Gel, *J. Am. Ceram. Soc.* 69 (1986) 464-467. <https://doi.org/10.1111/j.1151-2916.1986.tb07446.x>.
- [63] L. B. Skinner, S. R. Chae, C. J. Benmore, H. R. Wenk, P. J. M. Monteiro, Nanostructure of Calcium Silicate Hydrates in Cements, *Phys. Rev. Lett.* 104 (2010) 195502. <https://doi.org/10.1103/PhysRevLett.104.195502>.

- [64] J. J. Thomas, J. J. Chen, H. M. Jennings, D. A. Neumann, Ca–OH Bonding in the C–S–H Gel Phase of Tricalcium Silicate and White Portland Cement Pastes Measured by Inelastic Neutron Scattering, *Chem. Mater.* 15 (2003) 3813-3817. <https://doi.org/10.1021/cm034227f>.
- [65] W. Stumm, J. J. Morgan, *Aquatic Chemistry: Chemical Equilibria and Rates in Natural Waters*, John Wiley & Sons, New York, USA, 1996.
- [66] G. S. Pokrovski, J. Schott, F. Farges, J.-L. Hazemann, Iron (III)-silica interactions in aqueous solution: Insights from X-ray absorption fine structure spectroscopy, *Geochim. Cosmochim. Ac.* 67 (2003) 3559-3573. [https://doi.org/10.1016/S0016-7037\(03\)00160-1](https://doi.org/10.1016/S0016-7037(03)00160-1).
- [67] Y. Zhu, E. J. Elzinga, Formation of Layered Fe(II)-Hydroxides during Fe(II) Sorption onto Clay and Metal-Oxide Substrates, *Environ. Sci. Technol.* 48 (2014) 4937-4945. <https://doi.org/10.1021/es500579p>.
- [68] S. Zhou, E. S. Howard, J. Liu, N. H. Bashian, K. Nolan, S. Krishnamoorthy, G. M. Rangel, M.-T. Sougrati, G. K. S. Prakash, K. Page, B. C. Melot, Hydrothermal Preparation, Crystal Chemistry, and Redox Properties of Iron Muscovite Clay, *ACS Appl. Mater. Inter.* 9 (2017) 34024-34032. <https://doi.org/10.1021/acsami.7b08729>.
- [69] A. Peys, L. Arnout, T. Hertel, R. I. Iacobescu, S. Onisei, L. Kriskova, H. Rahier, B. Blanpain, Y. Pontikes, The use of ATR-FTIR spectroscopy in the analysis of iron-silicate inorganic polymers, *Proceedings of the 5th International Slag Valorisation Symposium*, Leuven, Belgium, April, 2017, p 385-388.
- [70] L. Machiels, L. Arnout, P. T. Jones, B. Blanpain, Y. Pontikes, Inorganic Polymer Cement from Fe-silicate Glasses: Varying the Activating Solution to Glass Ratio, *Waste Biomass Valori.* 5 (2014) 411-428. <https://doi.org/10.1007/s12649-014-9296-5>.